

Residual stresses in thermal barrier coatings: effects of interface asperity curvature/height and oxide thickness

Chun-Hway Hsueh ^{a,*}, Edwin R. Fuller Jr. ^b

^a *Metals and Ceramics Division, Oak Ridge National Laboratory, PO Box 2008, Oak Ridge, TN 37831-6068, USA*

^b *National Institute of Standards and Technology, Gaithersburg, MD 20899, USA*

Received 27 September 1999; received in revised form 21 December 1999

Abstract

The effects of curvature and height of the interface asperity on residual thermal stresses in a plasma-sprayed thermal barrier coating were numerically simulated. In the tip region of a convex asperity, the residual stress normal to the interface, σ_y is tensile in the ceramic top coat and increases with both curvature and height of the asperity. However, this residual tensile stress is lower for a periodic array of asperities than for an isolated asperity. The effects of thickness of the thermally grown oxide at the top coat–bond coat interface on residual thermal stresses were also numerically simulated. In the tip region of a convex asperity, σ_y in the ceramic top coat is tensile for a thin oxide but becomes compressive for a thick oxide. In the tip region of a concave asperity, σ_y in the ceramic top coat is compressive for a thin oxide and becomes less compressive for a thick oxide. The physical meaning of the above trend was qualitatively interpreted using an analytical model of three concentric circles. Published by Elsevier Science S.A.

Keywords: Residual stresses; Coating; Numerical simulations; Analytical modeling

1. Introduction

A typical plasma-sprayed thermal barrier coating (TBC) system consists of an oxidation-resistant metallic bond coat overlaid with a porous, thermally-insulating ceramic top coat (see Fig. 1) [1–4]. It has been found that a rough bond coat surface can increase the lifetime of a plasma-sprayed TBC system during thermal cycling in a turbine engine [3,5,6]. However, the residual thermal stresses in the system are affected by the asperities present at the top coat–bond coat interface [7–17]. Specifically, the residual stress normal to the interface, σ_y , would be zero if the interface is perfectly flat, but it becomes non-zero in the presence of interface asperities. When σ_y is tensile in the ceramic top coat, it may result in cracking and spallation of the top coat. The interface asperities can have various geometries with different curvatures and heights. An issue regarding the effects of the curvature and the height of the interface asperity on the residual stresses was hence raised. Also, an oxide

scale grows along the interface during high temperature exposure [2–6,18]. This thermally grown oxide (TGO) inevitably modifies the residual stresses in the system. Hence, the second issue is how the TGO thickness affects the residual stresses.

The purpose of the present study was to address the above two issues. To achieve this, the object oriented finite element analysis (OOF) [19] was utilized for numerical simulations. First, the effects of the asperity curvature were examined by simulating a convex semi-circular-top asperity and a convex rectangular-top asperity with the same height, and the effects of the asperity height were examined by simulating asperities with a semicircular top (or a rectangular top) and different heights. Second, a convex and concave semi-circular asperities with different TGO thicknesses were, respectively, simulated to examine effects of the TGO thickness on residual stresses. Third, a periodic array of convex and concave semicircular (or rectangular) asperities was simulated to examine effects of interaction between asperities on residual stresses. Finally, a simple analytical model of three concentric circles was used to explore the physical meaning of the trend of the TGO thickness effects on residual stresses.

* Corresponding author. Tel.: +1-865-5766586; fax: +1-865-5748445.

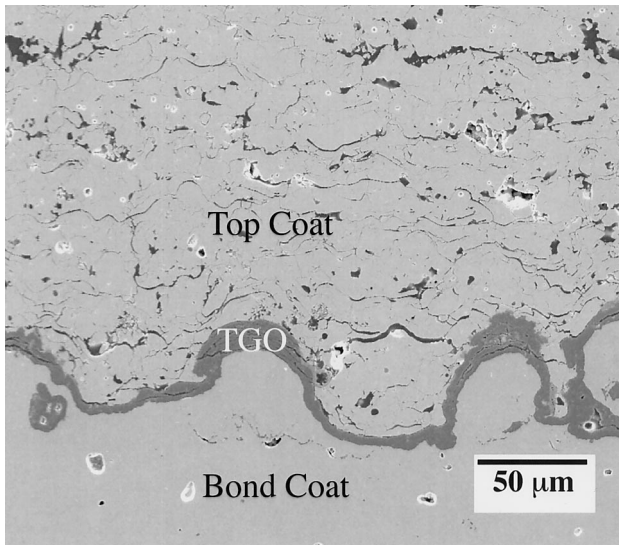


Fig. 1. The microstructure of a plasma sprayed ZrO_2 top coat– Al_2O_3 TGO–NiCrAlY bond coat system [4]. The René N5 substrate is not shown.

2. Numerical simulations and results

Numerical simulations were performed using OOF, which was uniquely designed to operate on microstructural images and has been run previously on both an actual cross-sectional microstructure and model microstructures of a plasma-sprayed TBC to obtain full-field residual stresses [4,20]. The thermal–mechanical properties pertinent to the air plasma-sprayed ZrO_2 top coat– α - Al_2O_3 TGO–vacuum plasma-sprayed Ni–22Cr–10Al–1Y bond coat–René N5 substrate system are listed in Table 1 [2,21]. The temperature change used in calculating the residual stresses was $-1125^\circ C$. It is noted that the TBC system is subjected to biaxial residual stresses in the plane parallel to the interface when interface asperities are not considered. The residual stress normal to the interface induced by interface asperities is expected to be much smaller than that parallel to the interface. Hence, while the simulation is a two-dimensional analysis, E should be replaced by $E/(1-\nu)$ in applying the plane-stress analysis, OOF, to the cross-section of the TBC system to account for the biaxial-stress in the TBC system [8,10,20,22] where E is Young's modulus and ν is Poisson's ratio.

Table 1

The thermal–mechanical properties of the plasma sprayed ZrO_2 top coat– Al_2O_3 TGO–NiCrAlY bond coat–René N5 substrate system

	Young's modulus, E (GPa)	Poisson's ratio, ν	CTE, α ($\times 10^{-6}/^\circ C$)
Porous top coat	50	0.1	10
Oxide scale	360	0.27	8
Bond coat	200	0.3	15.2
Substrate	213	0.25	14.5

2.1. Effects of curvature and height of interface asperity

Two sets of model microstructures were used in the present study to examine the effects of the curvature and the height of the interface asperity. Since these effects can be obscured by the presence of TGO at the interface, the TGO is not included in these two sets of model microstructures. In the first set, the top of the asperity is a semicircle with a radius a , and the height of asperity is controlled by adding a block at the base of the semicircle. The semicircular asperities with heights a , $2a$, and $3a$ are shown in Fig. 2(a–c), respectively. In the second set, the top of the asperity is flat such that the asperity has a rectangular shape, and the width of the asperity is $2a$. The rectangular asperities with heights a , $2a$, and $3a$ are shown in Fig. 2(d–f), respectively. In this case, the curvatures at the asperity top are $1/a$ and 0 , respectively, for semicircular and rectangular asperities.

The model microstructure was digitized to a portable pixel map (ppm) format. Using a uniform grid in OOF, each pixel in the ppm format corresponded to a grid in OOF, and each grid consisted of two triangular elements. The processed images shown in Fig. 2 consist of 64 082 elements each. Since the substrate (not shown in Figs. 1 and 2) was much thicker than the TBC, the thermal strain of the substrate (i.e. -0.0163) was used as the boundary condition at the right and the left edges of the image in Fig. 2 to constrain its distortion in the x -direction.

Using OOF, the predicted full-field residual stresses normal to the interface, σ_y , are also shown in Fig. 2(a–f). While effects of the asperity curvature can be obtained by comparing the results from the semicircular asperity with those from the rectangular asperity having the same height, effects of the asperity height can be obtained by examining the results from the semicircular (or rectangular) asperities with different heights. It can be seen that the curvature and the height of the asperity affect the residual stress field in the region of the asperity. Within the asperity, σ_y is tensile and it increases with both the curvature and the height of the asperity. The simulated results of σ_y within the top coat at the tip of the semicircular asperity and at the middle of the top of the rectangular asperity as functions of the

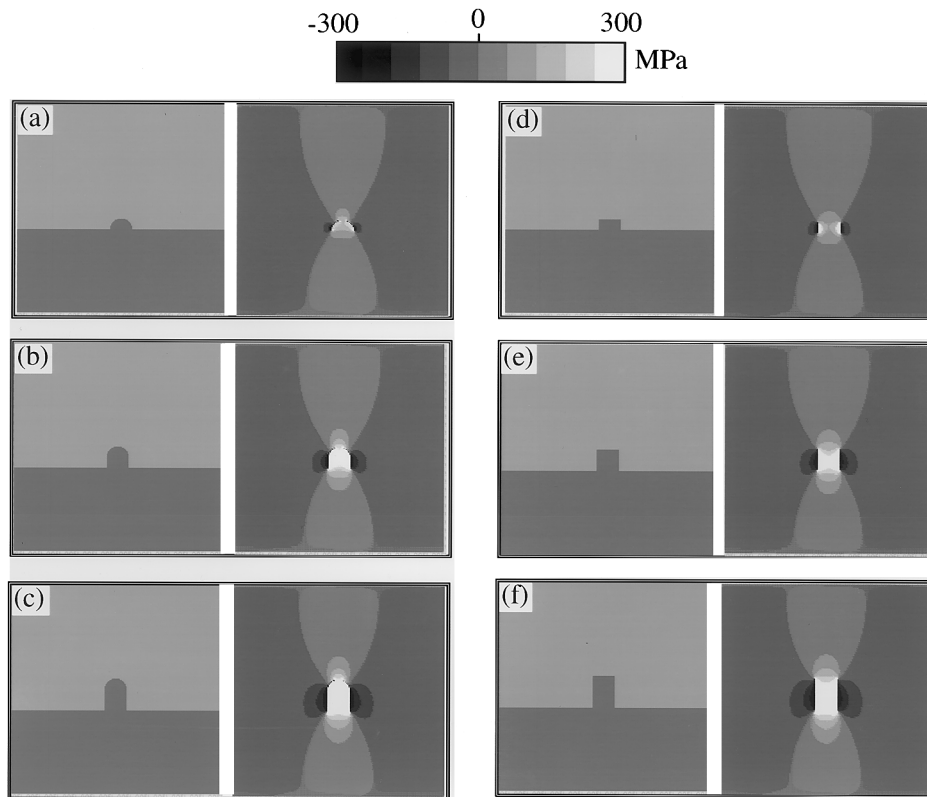


Fig. 2. The model microstructures and the simulated residual stress, σ_y , for the plasma-sprayed TBC system with a semicircular interface asperity having a height (a) a , (b) $2a$, and (c) $3a$, and with a rectangular interface asperity having a height (d) a , (e) $2a$, and (f) $3a$.

asperity height are shown in Fig. 3. For convenience, a subscript, o, is added to define σ_y at the above mentioned positions. It can be seen that σ_{y_o} increases with both the curvature and the height of the asperity. The thickness ratio of the top coat to the bond coat for the model microstructures adopted in the present study is 1.5. Since the thermal strain of the substrate was used to constraint the distortion of the TBC in the x -direction, the calculated σ_{y_o} is independent of the thickness ratio of the top coat to the bond coat when the asperity is remote from the free surface of the top coat.

It is noted that the effects of curvature and height of interface asperities have also been studied by assuming a sinusoidal interface with varying wavelength and amplitude [17]. The general trend exhibits that the magnitude of the residual stress normal to the interface increases with increasing wrinkling of the interface [17] which is in agreement with the present result. It is also noted that corners were introduced by using the rectangular asperity in the present study which would result in singularities. However, the stresses used for comparison are not at corners, and different sizes of mesh have been used in the OOF analysis to ensure convergence of the simulated result for σ_{y_o} .

2.2. Effects of the TGO thickness

The residual stress states associated with a convex and a concave interface asperities are different. To examine the effects of the TGO thickness on residual stresses, convex and concave semicircular asperities are considered, respectively. The semicircular asperity has a

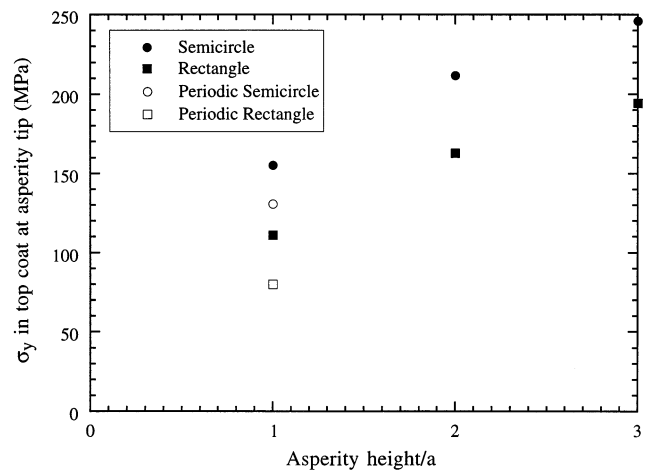


Fig. 3. Simulated results of σ_y within the top coat at the tip of the semicircular asperity and at the middle of the top of rectangular asperity as functions of the asperity height. The stress reduction for a periodic array of asperities is also shown at the asperity height of a .

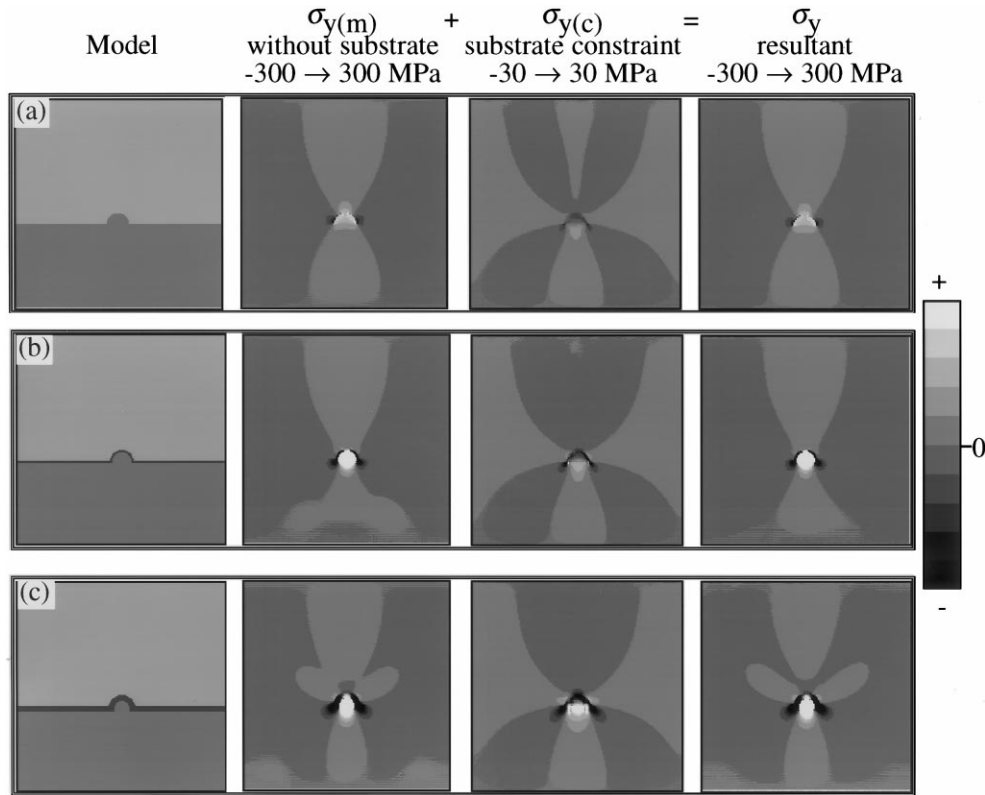


Fig. 4. The model microstructures and the simulated residual stresses, $\sigma_{y(m)}$, $\sigma_{y(c)}$, and σ_y , for the plasma-sprayed TBC system with a convex semicircular interfacial asperity having a radius, a , and a TGO thickness of (a) 0, (b) $0.23a$, and (c) $0.72a$.

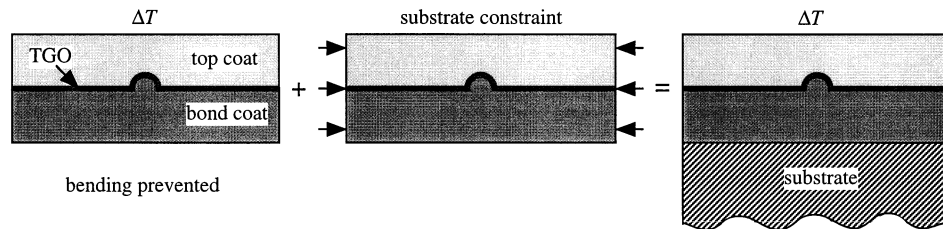


Fig. 5. Schematic showing the residual stress in the TBC system can be decomposed into two components: the one due to the thermal-mechanical mismatch among the top coat, the TGO, and the bond coat, and the one due to the substrate constraint imposed on the coating system.

radius a and the TGO has a variable thickness t . It is noted that oxidation generally induces a volume expansion. It can be readily incorporated in the OOF analysis by replacing the coefficient of thermal expansion (CTE) of the oxide scale by an effective CTE, such that the thermal strain due to the effective CTE equals the sum of the thermal strain due to the actual CTE and the oxidation strain. However, this was not done here because the oxidation strain for converting the bond coat to the oxide scale is not well documented.

2.2.1. Convex asperities

A convex semicircular asperity without TGO ($t/a = 0$), with a relatively thin TGO ($t/a = 0.23$), and with a relatively thick TGO ($t/a = 0.72$) are shown in Fig. 4(a–c), respectively. To explore the physical insights of

the TGO thickness effects on residual stresses, it is instructive to decompose the residual stress, σ_y , into two components: (1) $\sigma_{y(m)}$, the one due to the thermal-mechanical mismatch among the top coat, the TGO, and the bond coat, and (2) $\sigma_{y(c)}$, the one due to the substrate constraint imposed on the coating system (see Fig. 5). Running OOF, these two components can be obtained using the following procedures.

First, using the procedures described in Section 2.1, the residual stress in the y -direction, σ_y , can be obtained. In this case, the thermal strain of the substrate, -0.0163 , was imposed as the boundary condition at the right and the left edges of the image of the coating system to constrain its distortion in the x -direction. After equilibrating under $\Delta T = -1125^\circ\text{C}$, the top coat, the TGO, and the bond coat are, respectively, subjected

to uniform elastic strains in the x -direction at the right and the left edges of the image. For example, these uniform elastic strains are -0.00502 , -0.00727 , and 0.00082 , respectively, for the top coat, the TGO, and the bond coat when $t/a = 0.23$ (Fig. 4(b)). Second, the right and the left edges of the image are, respectively, set to have the same displacement in the x -direction (i.e. no bending in the coating system). This is achieved by using the ‘enslave’ boundary condition in the OOF menus. Using $\Delta T = -1125^\circ\text{C}$, the residual stress obtained in the y -direction is $\sigma_{y(m)}$. In this case, unlike the above, the coating system is free of the substrate constraint; however, the top coat, the TGO, and the bond coat are, respectively, subjected to uniform elastic strains in the x -direction at the right and the left edges of the image because of the CTE mismatch. For example, these uniform elastic strains are -0.00426 , -0.00651 , and 0.00158 , respectively, for the top coat, the TGO, and the bond coat when $t/a = 0.23$ (Fig. 4(b)). Third, the difference between the two sets of elastic strain is due to the substrate constraint effect. For example, the elastic strain in the x -direction due to substrate constraint is -0.00076 when $t/a = 0.23$ (Fig. 4(b)) which is then imposed as the boundary condition at the right and the left edges of the image to constrain its distortion in the x -direction. Using $\Delta T = 0$, the residual stress thus obtained in the y -direction is $\sigma_{y(c)}$.

Using the above procedures, the corresponding $\sigma_{y(m)}$, $\sigma_{y(c)}$, and σ_y are also shown in Fig. 4(a–c). It can be seen that the full-field residual stress of $\sigma_{y(m)}$ is similar to that of σ_y . Hence, compared to $\sigma_{y(c)}$, $\sigma_{y(m)}$ dominates the resultant σ_y (see Fig. 4). This is due to the fact that the substrate and the bond coat have the similar CTEs (see Table 1), and the substrate constraint effect imposed on the coating system is insignificant. However, the contribution of $\sigma_{y(c)}$ to the resultant σ_y increases with the increase in the TGO thickness. The simulated

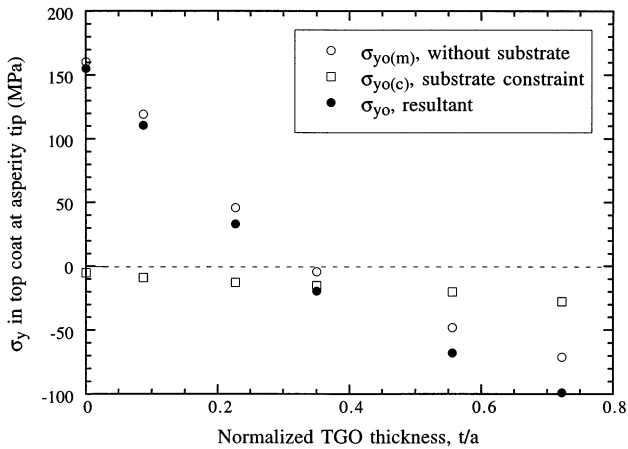


Fig. 6. The residual stresses within the top coat at the tip of a convex semicircular asperity, $\sigma_{yo(m)}$, $\sigma_{yo(c)}$, and σ_{yo} , as functions of the TGO thickness.

residual stresses within the top coat at the tip of the semicircular asperity (i.e. $\sigma_{yo(m)}$, $\sigma_{yo(c)}$, and σ_{yo}) are plotted in Fig. 6 as functions of the TGO thickness. Whereas $\sigma_{yo(m)}$ is tensile for thin TGOs and becomes compressive for thick TGOs, $\sigma_{yo(c)}$ is always compressive and its magnitude increases with the TGO thickness. Two general features can be observed in Fig. 4. First, the tensile stress state, $\sigma_{y(m)}$ (and σ_y), moves from the tip to the side of the asperity as the TGO grows. Second, the stress state, $\sigma_{y(m)}$, far above the asperity persists to be tensile even when σ_{yo} becomes compressive for thick TGOs. These two features are explained as follows.

First, the polar coordinates with its origin located at the center of the semicircular asperity can be used to facilitate visualizing the stress state in the top coat close to the asperity. The bond coat has a greater CTE than the top coat. Hence, in the absence of the TGO, the residual stress in the top coat around the asperity is tensile in the radial direction and compressive in the tangential direction. When σ_y is considered, it becomes the radial stress at the tip of the asperity and becomes the tangential stress at the side of the asperity. Hence, σ_y is tensile and compressive, respectively, at the tip and the side of the asperity. The TGO has the lowest CTE in the coating system. Hence, when the TGO is sufficiently thick, the residual stress in the top coat around the asperity becomes compressive in the radial direction and tensile in the tangential direction. This would cause σ_y to be compressive and tensile, respectively, at the tip and the side of the asperity. As a result, the tensile stress state, $\sigma_{y(m)}$ (and σ_y), moves from the tip to the side of the asperity as the TGO grows.

Second, the stress state, $\sigma_{y(m)}$, far above the asperity can be visualized by dividing the model microstructure into vertical thin strips. Compared to other strips, the strip passing the convex asperity has a greater bond coat area and a smaller top coat area. Since the bond coat has a greater CTE than the top coat, the strip passing the convex asperity has a greater effective CTE than other strips. As a result, in the strip passing the convex asperity, the far field residual stress, $\sigma_{y(m)}$, above the asperity is always tensile during cooling despite the fact that the near field stress $\sigma_{yo(m)}$ becomes compressive for thick TGOs.

2.2.2. Concave asperities

A concave semicircular asperity without TGO ($t/a = 0$), with a relatively thin TGO ($t/a = 0.24$), and with a relatively thick TGO ($t/a = 0.72$) are shown in Fig. 7(a–c), respectively. Like the residual stress, σ_y , in the case of convex semicircular asperity, σ_y in the case of concave asperity can also be decomposed into two components: $\sigma_{y(m)}$ and $\sigma_{y(c)}$. Using OOF and the procedures described in Section 2.2.1, the corresponding simulated results for $\sigma_{y(m)}$, $\sigma_{y(c)}$, and σ_y are also

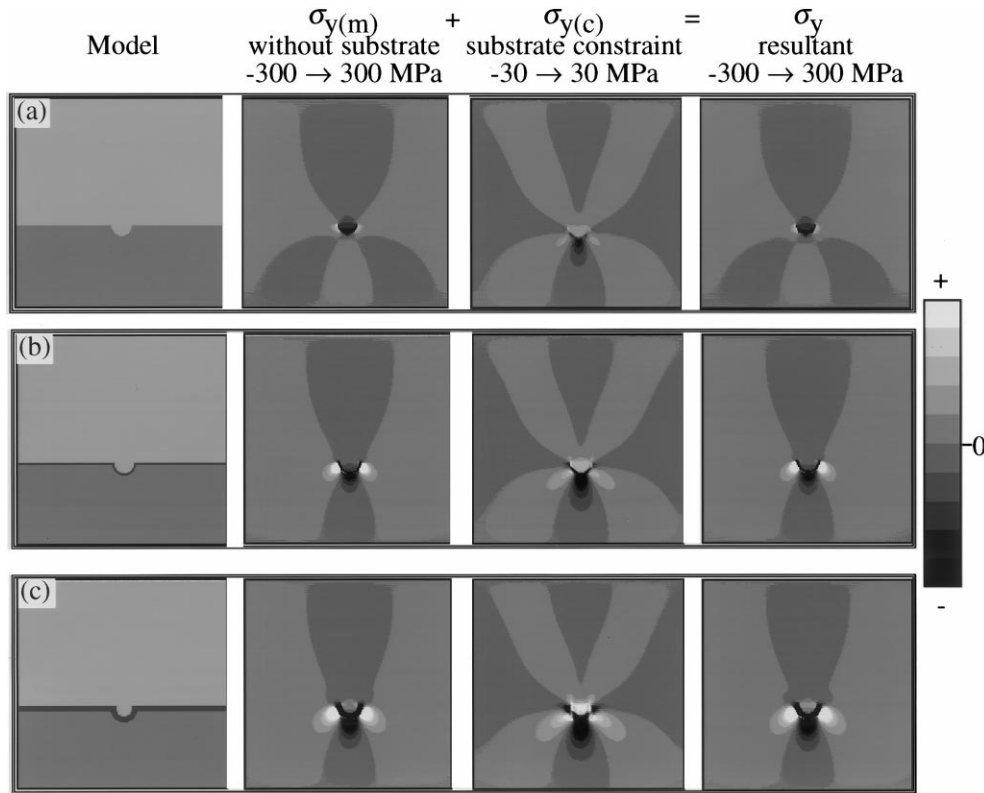


Fig. 7. The model microstructures and the simulated residual stresses, $\sigma_{y(m)}$, $\sigma_{y(c)}$, and σ_y , for the plasma-sprayed TBC system with a concave semicircular interfacial asperity having a radius, a , and a TGO thickness of (a) 0, (b) $0.24a$, and (c) $0.72a$.

shown in Fig. 7(a–c). The resultant σ_y is dominated by $\sigma_{y(m)}$ (see Fig. 7). The residual stresses within the top coat at the tip of the semicircular asperity (i.e. $\sigma_{y0(m)}$, $\sigma_{y0(c)}$, and σ_{y0}) are plotted in Fig. 8 as functions of the TGO thickness. For the range of the TGO thickness considered in the present study, $\sigma_{y0(m)}$ is always compressive and $\sigma_{y0(c)}$ is always tensile. As the TGO thickness increases, the magnitudes of $\sigma_{y0(m)}$ and $\sigma_{y0(c)}$ decrease and increase, respectively. It is noted that in the top coat, a tensile σ_y region above the asperity is observed for thick oxides (see σ_y in Fig. 7(c)) although σ_y remains compressive at the asperity tip. Specifically, this tensile σ_y reaches 100 MPa for the case considered in Fig. 7(c) which could result in cracking in the ceramic top coat.

2.3. Effects of interaction between asperities

To examine the effects of interaction between asperities on residual stresses, periodical arrays of convex and concave semicircular asperities with radius a (Fig. 9(a)) and of square asperities with length $2a$ and separation $2a$ (Fig. 9(b)) were considered. In this case, the asperity amplitude is a from the centerline of the interface for both arrays of asperities.

A uniform grid was also used to simulate the model microstructures in Fig. 9, and the processed images

consisted of 64 082 elements each. The corresponding full-field residual stress, σ_y , are also shown in Fig. 9. The simulated results of σ_{y0} are 130.8 and -240.6 MPa, respectively, for the semicircular convex and concave asperities, and are 80 and -185 MPa, respectively, for the rectangular convex and concave asperities. These tensile stresses σ_{y0} (i.e. 130.8 and 80 MPa) for convex asperities are also shown in Fig. 3 at

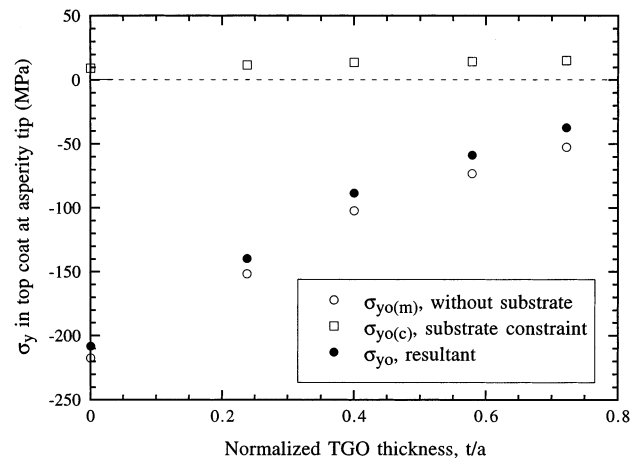


Fig. 8. The residual stresses within the top coat at the tip of a concave semicircular asperity, $\sigma_{y0(m)}$, $\sigma_{y0(c)}$, and σ_{y0} , as functions of the TGO thickness.

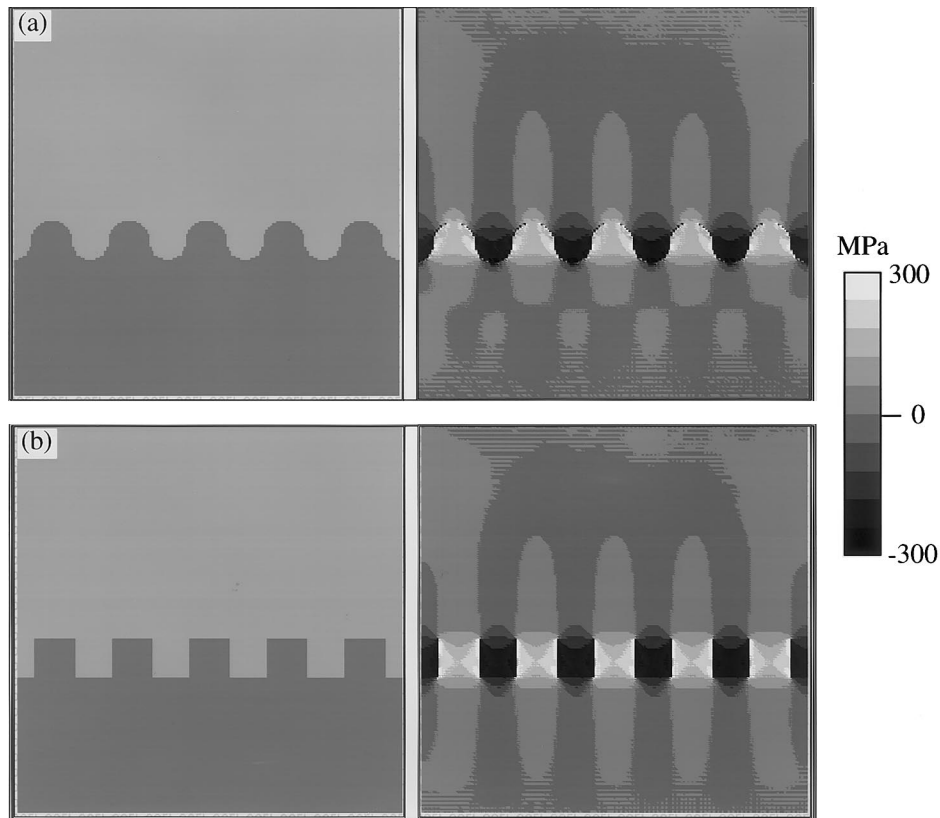


Fig. 9. The model microstructures and the simulated residual stress, σ_y , for the plasma-sprayed TBC system with a periodic array of (a) convex and concave semicircular asperities with radius a , and (b) square asperities with length $2a$ and separation $2a$.

an asperity height value of a to compare with those due to an isolated asperity.

3. Analytical modeling and results

A two-concentric-circles model has been used previously to study the effects of the surface curvature of the substrate on oxidation behavior [7,17]. To explore the physical meaning of the numerically simulated (or experimental) results, a simple analytical model bearing the essential features of the simulated geometry (or specimen) is required. The essential features in the present case are the top coat–TGO interface, the TGO–bond coat interface, convex and concave asperities, and the TGO thickness. To include the above features, a simple three-concentric-circles model is adopted in the present study which is described as follows.

A circular region of phase 1 with a radius a is surrounded by a concentric annulus of phase 2 with an outer radius b which is then surrounded by another concentric annulus of phase 3 with an outer radius c (see Fig. 10). Whereas phases 1, 2, and 3 are designated respectively as the bond coat, the TGO, and the top coat in modeling a convex asperity, they are designated

respectively as the top coat, the TGO, and the bond coat in modeling a concave asperity. In both cases, the two interfaces are located at $r = a$ and b , and the TGO thickness is dictated by $b - a$. It has been shown in Section 2.2 that the substrate constraint effect on the coating system is insignificant because the substrate and the bond coat have the similar CTEs. Hence, excluding the substrate from the three-concentric-circles model is appropriate in analyzing the residual thermal stresses in the TBC system.

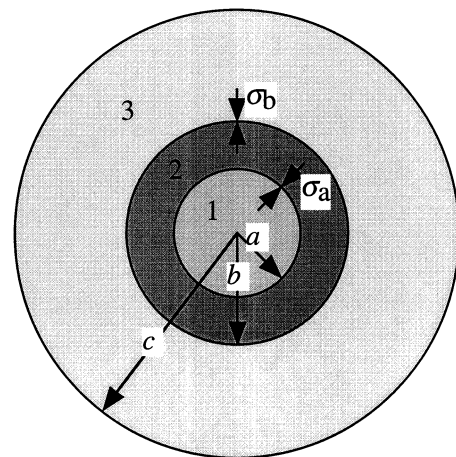


Fig. 10. A schematic showing the three-concentric-circles model.

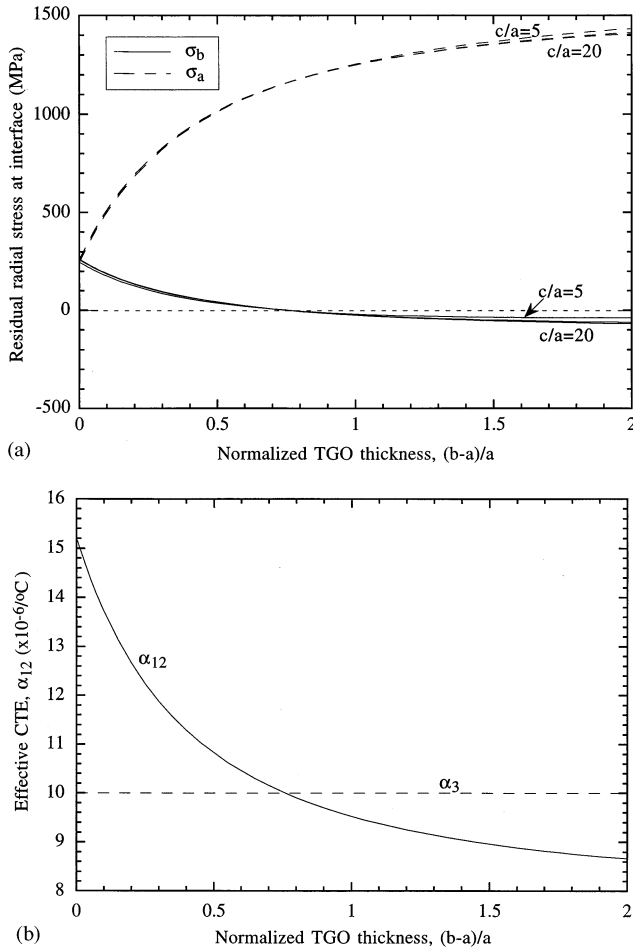


Fig. 11. (a) The residual radial stress at the TGO/bond coat interface, σ_a , and at the top coat–TGO interface, σ_b , and (b) the effective CTE, α_{12} , for the region $r < b$, and the CTE of top coat, α_3 , as functions of the normalized TGO thickness, $(b-a)/a$, at different c/a ratios for a convex asperity.

3.1. Analyses

Residual thermal stresses develop during the temperature change in the system because of the thermal–mechanical mismatch among the three phases. The stresses can be determined by the procedure of first allowing the three phases to exhibit unconstrained differential thermal strains during the temperature change, ΔT . Then, radial stresses, σ_a and σ_b , are placed at the interfaces, $r = a$ and b , respectively, to restore the displacement continuity at the two interfaces. It can be derived that the interfacial radial stresses, σ_a and σ_b , are [23]

$$\sigma_a = \frac{P_1 E_2 (\alpha_{23} - \alpha_1) \Delta T}{P_1 P_2 - P_3 P_4} \quad (1)$$

$$\sigma_b = \frac{P_2 E_2 (\alpha_3 - \alpha_{12}) \Delta T}{P_1 P_2 - P_3 P_4} \quad (2)$$

where the parameters, P_1 , P_2 , P_3 , and P_4 , are given by

$$P_1 = \frac{b^2 + a^2}{b^2 - a^2} - \nu_2 + \frac{E_2}{E_3} \left(\frac{c^2 + b^2}{c^2 - b^2} + \nu_3 \right) \quad (3a)$$

$$P_2 = \frac{b^2 + a^2}{b^2 - a^2} + \nu_2 + \frac{E_2 (1 - \nu_1)}{E_1} \quad (3b)$$

$$P_3 = \frac{2a^2}{b^2 - a^2} \quad (3c)$$

$$P_4 = \frac{2b^2}{b^2 - a^2} \quad (3d)$$

subscripts 1, 2, and 3 for the elastic constants denote phases 1, 2, and 3, respectively, and where α_1 and α_3 are the CTEs of phases 1 and 3, α_{12} has the physical meaning of the effective CTE in the region of $r < b$ which is a function of properties of phases 1 and 2, and α_{23} has the physical meaning of the effective CTE in the region of $a < r < c$ which is a function of properties of phases 2 and 3, such that

$$\alpha_{12} = \alpha_2 + \frac{P_3 (\alpha_1 - \alpha_2)}{P_2} \quad (4)$$

$$\alpha_{23} = \alpha_2 + \frac{P_4 (\alpha_3 - \alpha_2)}{P_1} \quad (5)$$

3.2. Results

The thermal–mechanical properties of the TBC system listed in Table 1 and $\Delta T = -1125^\circ\text{C}$ were used, and E was replaced by $E/(1 - \nu)$ before it was substituted into the analytical solutions due to the biaxial stress state in the TBC system as discussed in section 2.

3.2.1. Convex asperities

For a convex asperity, phases 1, 2, and 3 correspond to the bond coat, the TGO, and the top coat, respectively. The residual radial stresses at $r = a$ and b (i.e. σ_a and σ_b) as functions of the normalized TGO thickness, $(b-a)/a$, are shown in Fig. 11(a) for $c/a = 5, 10,$ and 20 . In this case, σ_b corresponds to σ_y in the top coat at the tip of a convex asperity. The stresses are not sensitive to c/a when $c/a \geq 5$. The results for $c/a = 10$ almost overlap with those for $c/a = 20$, and can't be distinguished in Fig. 11(a). While σ_a is tensile and increases with the TGO thickness (which agrees with the trend in Fig. 4), σ_b is tensile when $(b-a)/a < \sim 0.75$ and becomes compressive when $(b-a)/a > \sim 0.75$. The effective CTE, α_{12} , as a function of the normalized TGO thickness, $(b-a)/a$, is shown in Fig. 11(b). It is noted that α_{12} is independent of c (see Eq. (4)). The CTE of phase 3, α_3 ($= 10 \times 10^{-6}/^\circ\text{C}$), is also shown in Fig. 11(b). It can be seen that $\alpha_{12} > \alpha_3$ when $(b-a)/a < \sim 0.75$ which, in turn, results in a tensile residual radial stress at $r = b$ during cooling. Conversely, $\alpha_{12} < \alpha_3$ when $(b-a)/a > \sim 0.75$ which, in turn, results in a compressive residual radial stress at $r = b$ during cooling.

3.2.2. Concave asperities

For a concave asperity, phases 1, 2, and 3 correspond to the top coat, the TGO, and the bond coat, respectively. The residual radial stresses at $r = a$ and b as functions of the normalized TGO thickness, $(b - a)/a$, are shown in Fig. 12(a) at different c/a ratios. In this case, σ_a corresponds to σ_y in the top coat at the tip of a concave asperity. The stresses are not sensitive to c/a when $c/a \geq 10$. While σ_b is compressive and its magnitude increases with the TGO thickness for $c/a \geq 10$ (which agrees with the trend in Fig. 7), σ_a becomes less compressive with the increasing TGO thickness and the decreasing c/a for the dimension considered in Fig. 12(a). The effective CTE, α_{23} , as a function of the normalized TGO thickness, $(b - a)/a$, is shown in Fig. 12(b) at different c/a ratios. The CTE of phase 1, α_1 ($= 10 \times 10^{-6}/^\circ\text{C}$), is also shown. It can be seen that $\alpha_{23} > \alpha_1$ for the dimension considered in Fig. 12(b). However, the difference between α_{23} and α_1 decreases with the increasing TGO thickness and the decreasing

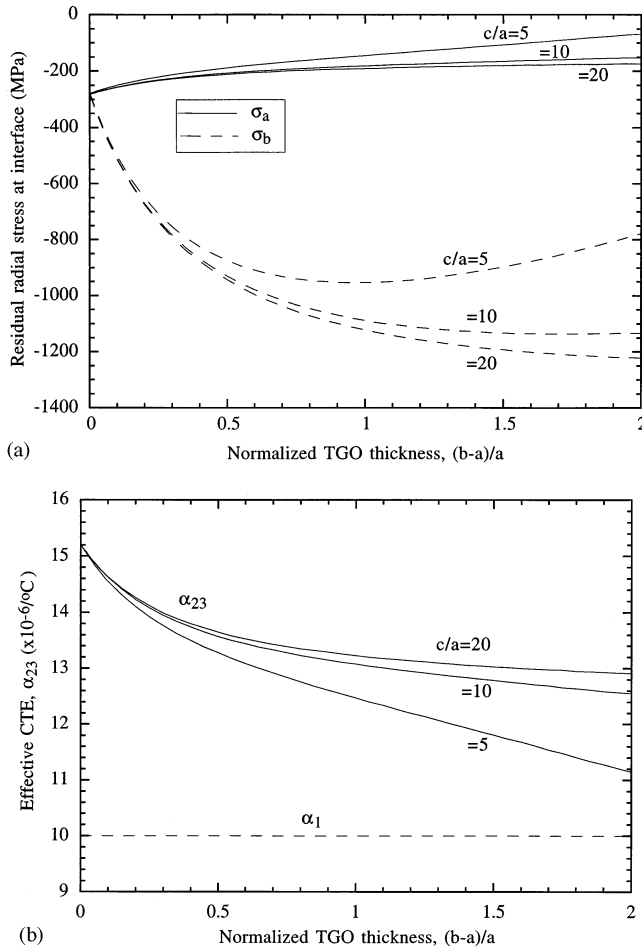


Fig. 12. (a) The residual radial stress at the top coat-TGO interface, σ_a , and at the TGO-bond coat interface, σ_b , and (b) the effective CTE, α_{23} , for the region $a < r < c$, and the CTE of top coat, α_1 , as functions of the normalized TGO thickness, $(b - a)/a$, at different c/a ratios for a concave asperity.

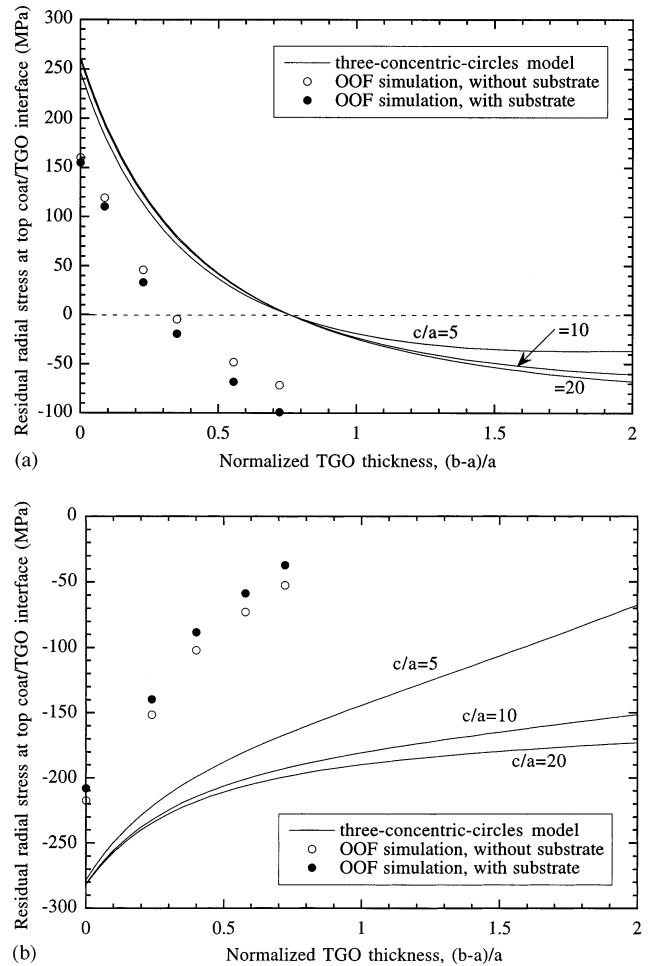


Fig. 13. Comparison between simulated results and analytical results for the residual stress normal to the interface within the top coat and at the tip of (a) a convex asperity, and (b) a concave asperity.

c/a . Compared to Fig. 11(b), Fig. 12(b) shows that the decrease in α_{23} is much slower than the decrease in α_{12} when the TGO thickness increases. This is due to the fact that the bond coat for a concave asperity (i.e. phase 3 in Fig. 10) has a much greater area than that for a convex asperity (i.e. phase 1 in Fig. 10) in the three-concentric-circles model, and the effect of the TGO thickness on the effective CTE is much weaker for a concave asperity than for a convex asperity.

3.2.3. Comparison with simulated results

Despite the different geometries adopted in numerical simulations (Fig. 5) and analytical modeling (Fig. 10) for the TBC system, the predicted residual stresses normal to the interface in the top coat and at the asperity tip as functions of the normalized TGO thickness, $(b - a)/a$, are shown in Fig. 13(a–b), respectively, for convex and concave asperities. For numerical simulations, results for the coating system without substrate constraint and with substrate constraint are both shown. For the three-concentric-circles analytical

model, results for different c/a ratios are shown. It can be seen that the variations of these residual stresses with the TGO thickness are qualitatively the same between numerical simulations and analytical modeling.

4. Conclusions

The effects of (1) the curvature and the height of the interface asperity, (2) the thickness of the thermally grown oxide (TGO), and (3) interaction between asperities on residual thermal stresses in a plasma-sprayed TBC system were numerically simulated. The following qualitative trends were concluded from the present numerical simulations.

1. In the absence of TGO, the residual stress normal to the interface, σ_y , in the tip region of convex asperity is tensile within the top coat which increases with both the curvature and the height of the asperity (Figs. 2 and 3).

2. The residual stress, σ_y , can be decomposed into two components: (1) $\sigma_{y(m)}$, the one due to the thermal-mechanical mismatch among the top coat, the TGO, and the bond coat, and (2) $\sigma_{y(c)}$, the one due to the substrate constraint imposed on the coating system (Fig. 5). Whereas $\sigma_{y(m)}$ dominates, the contribution of $\sigma_{y(c)}$ to the resultant σ_y increases with the TGO thickness.

3. The residual stress, σ_y , at the asperity tip within the top coat is defined as σ_{y0} . For a convex asperity, σ_{y0} is tensile for thin TGOs but becomes compressive for thick TGOs (Fig. 6). The tensile stress state, σ_y , moves from the tip to the side of the asperity as the TGO grows (Fig. 4). Also, the stress state, σ_y , far above the asperity persists to be tensile even when σ_{y0} becomes compressive for thick TGOs (Fig. 4).

4. For a concave asperity, σ_{y0} in the ceramic top coat is compressive for thin TGOs and becomes less compressive for thick TGOs (Figs. 7 and 8). However, σ_y can become tensile above the asperity tip and within the top coat for thick TGOs (see σ_y in Fig. 7c).

5. In the presence of multiple asperities, σ_{y0} is reduced due to the interaction between asperities (Figs. 3 and 9).

The physical meaning of the trend of the variations of residual stresses, σ_y , with the TGO thickness was qualitatively interpreted using an analytical model of three concentric circles. Finally, it is noted that the present study aims at the qualitative trend of effects of interface asperities and TGO thickness on residual stresses, and the elastic solution is used. Including non linearity and creep in the finite element modeling, residual stresses in the TBC have been analyzed elsewhere [14].

Acknowledgements

The authors thank Drs P.F. Becher, P.F. Tortorelli, M.J. Lance, T.J. Chuang, and E.J. Garboczi for reviewing the manuscript. CHH acknowledges jointly support of the U.S. Department of Energy, Division of Materials Sciences, Office of Basic Energy Sciences, and Assistant Secretary for Energy, Efficiency and Renewable Energy, Office of Industrial Technologies, Advanced Turbine Systems Program, under contract DE-AC05-96OR22464 with Lockheed Martin Energy Research Corp. ERF acknowledges support of the Alexander von Humboldt Foundation.

References

- [1] R.A. Miller, *Surf. Coat. Technol.* 30 (1) (1987) 1–11.
- [2] W.Y. Lee, D.P. Stinton, C.C. Berndt, F. Erdogan, Y.D. Lee, Z. Mutasim, *J. Am. Ceram. Soc.* 79 (12) (1996) 3003–3012.
- [3] J.A. Haynes, E.D. Rigney, M.K. Ferber, W.D. Porter, *Surf. Coat. Technol.* 86–87 (1996) 102–108.
- [4] C.H. Hsueh, J.A. Haynes, M.J. Lance, P.F. Becher, M.K. Ferber, E.R. Fuller Jr, S.A. Langer, W.C. Carter, W.R. Cannon, *J. Amer. Ceram. Soc.* 82 (4) (1999) 1073–1075.
- [5] D.J. Wortman, B.A. Nagaraj, E.C. Duderstadt, *Mater. Sci. Eng.* A121 (1989) 433–440.
- [6] J.T. DeMasi-Marcin, K.D. Sheffler, S. Bose, *J. Eng. Gas Turbines Power* 112 (1990) 521–526.
- [7] C.H. Hsueh, A.G. Evans, *J. Appl. Phys.* 54 (11) (1983) 6672–6686.
- [8] A.G. Evans, G.B. Crumley, R.E. Demaray, *Oxid. Metals* 20 (5/6) (1983) 193–216.
- [9] G.C. Chang, W. Phucharoen, R.A. Miller, *Surf. Coat. Technol.* 30 (1987) 13–28.
- [10] H. Gao, *Int. J. Solids Structures* 28 (6) (1991) 703–725.
- [11] V.K. Tolpygo, H.J. Grabke, *Oxid. Metals* 41 (5/6) (1994) 343–364.
- [12] J.K. Wright, R.L. Williamson, R.M. Cannon, *Mater. Sci. Eng.* A230 (1997) 202–212.
- [13] M.Y. He, A.G. Evans, J.W. Hutchinson, *Mater. Sci. Eng.* A245 (1998) 168–181.
- [14] A.M. Freborg, B.L. Ferguson, W.J. Brindley, G.J. Petrus, *Mater. Sci. Eng.* A245 (1998) 182–190.
- [15] J. Chao, J.L. González-Carrasco, *Mater. Sci. Eng.* A230 (1997) 39–48.
- [16] J. Cheng, E.H. Jordan, B. Barber, M. Gell, *Acta Mater* 46 (16) (1998) 5839–5850.
- [17] X.Y. Gong, D.R. Clarke, *Oxid. Metals* 50 (5/6) (1998) 355–377.
- [18] B.A. Pint, I.G. Wright, W.Y. Lee, Y. Zhang, K. Prüner, K.B. Alexander, *Mater. Sci. Eng.* A245 (1998) 201–211.
- [19] S.A. Langer, W.C. Carter, E.R. Fuller, *Object Oriented Finite Element Analysis for Materials Science: Version 1.0*, National Institute of Standards and Technology, Nov. 1998.
- [20] C.H. Hsueh, P.F. Becher, E.R. Fuller Jr, S.A. Langer, W.C. Carter, *Materials Science Forum*, Vols. 308–311 (1999) 442–449.
- [21] R.V. Hillery, B.H. Pilsner, R.L. McKnight, T.S. Cook, M.S. Hartle, *Thermal barrier coating life prediction model development*, NASA Contractor Report 180807 (1988).
- [22] R.J. Christensen, V.K. Tolpygo, D.R. Clarke, *Acta Mater.* 45 (4) (1997) 1761–1766.
- [23] C.H. Hsueh, E.R. Fuller, Jr., *Scripta Materialia*, in press.